Draft: The Atacama Cosmology Telescope: SZ-based masses of IR-selected cluster candidates from the SHELA survey

Brittany Fuzia,[1]* Lalitwadee Kawinwanichakij,[2] Eli Rykoff,[3] Nicola Mehrtens,[2]
ACT and SHELA collaborators, including Kevin Huffenberger,[1] Casey Papovich[2],
Simone Aiola, Bruce Partridge, Cristóbal Sifón

[1] *Dept of Physics, Florida State University, Tallahassee, FL 32301, USA*
[2] *Dept of Physics and Astronomy, Texas A&M University, College Station, TX 77843, USA*
[3] *SLAC National Accelerator Laboratory, Menlo Park, CA 94025, USA*

ABSTRACT

We analyze the stacked Sunyaev-Zel'dovich (SZ) temperature decrement for an infrared-selected sample of galaxy cluster candidates from the Spitzer-HETDEX Exploratory Large Area (SHELA) Survey. The clusters are found in combined optical and infrared SHELA data using the redMaPPer algorithm. We separate the sample into three richness bins: $10 \leq \lambda < 20$, $20 \leq \lambda < 30$, and $\lambda \geq 30$. From the lowest to highest richness sample, the average redshifts are 0.80, 0.73, and 0.70. IR selection allows us to probe clusters at higher redshifts than typical with optically-selected samples, with objects less massive than those typical with SZ surveys. In the stacking analysis, Atacama Cosmology Telescope (ACT) measurements show a temperature decrement at 148 GHz. We attribute excess emission at the 220 GHz SZ null to dust emission from the cluster member galaxies. We correct for dust emission in the 148 GHz stack using the 220 GHz profile as the dust template. We extrapolate the 220 GHz signal to 148 GHz to based on a dust spectral energy distribution (SED) fit to data from the Herschel Stripe 82 (HerS) survey. We use a Markov Chain Monte Carlo to clean our decrement using the extrapolated 220 GHz dust profile and simultaneously fit for the cluster mass, using a universal galaxy cluster pressure profile for the average SZ signal. We find a mean mass of $M_{500} = (1.0 \pm 0.6) \times 10^{13} M_{\odot}$, $(2.3 \pm 1.2) \times 10^{13} M_{\odot}$, and $(5.6 \pm 1.6) \times 10^{13}$ $M_{\odot}$, respectively for the poorest and richest bins. These masses are 1.1, 1.4, and 3.5 times larger than what we find when neglecting the dust correction, indicating substantial fill-in of the SZ decrement from the cluster dust emission, up to **75 percent in terms of** Y_{500}**, although with large uncertainty.** We compare our SZ masses to two redMaPPer-based cluster scaling relations for richness and find that the SZ mass is lower than predicted by the richness, even after correcting for dust emission. Part of the discrepancy may be due to a differing interpretation of richness for selection in the infrared.

Key words:

1 INTRODUCTION

Clusters of galaxies are the largest gravitationally bound structures in the universe. They make powerful cosmological probes because they sample the maxima of the primordial density field. Various cluster observables relate to each other with scaling laws and these laws make clusters useful tools to gain insight into large-scale structure, galaxy evolution, dark matter dynamics, and cosmological parameters (Voit 2005; Giodini et al. 2013). The thermal Sunyaev-Zel'dovich (SZ) spectral distortion of the Cosmic Microwave Background (CMB) allows for indirect measurements of one of the most important observables—total galaxy cluster mass—and can identify clusters to high redshift (Sunyaev & Zeldovich 1972;

---

* E-mail: bjf13d@my.fsu.edu

Carlstrom et al. 2002). The SZ effect occurs when CMB photons scatter from the hot electron gas in the intracluster medium. Fewer than ~1 percent of photons interact and gain energy through inverse Compton scattering, altering the observed CMB spectrum and resulting in a characteristic spectral dependence for the SZ effect: a flux decrement for frequencies below 217 GHz and a flux increment for higher frequencies (Birkinshaw 1999; Carlstrom et al. 2002). The magnitude of the effect is proportional to the Comptonization parameter (the integrated electron pressure), and the pressure is proportional to the depth of the gravitational potential well. Therefore the amplitude of the SZ signal depends on the mass of the cluster. Using the SZ effect for cosmology requires an understanding of this relationship between halo mass and the SZ observable, which is often expressed as the Comptonization parameter integrated over the cluster's solid angle. Since the SZ effect is a distortion of the CMB's spectrum, the signal does not decrease with distance the way that the cluster brightness does, and so the SZ effect is an efficient way to find high-redshift clusters, limited only by the mass of the cluster and the sensitivity of the telescope.

At high mass, $M \gtrsim 10^{15}$ $M_\odot$, current SZ searches can already find halos efficiently at all redshifts, but at lower mass, $M \lesssim 10^{14}$ $M_\odot$, it becomes more difficult. These lower mass halos are interesting because their smaller potential wells have a harder time holding onto their gas, and they are laboratories for star formation and AGN feedback (Liu et al. 2015; Laganá et al. 2013). Although studies of low mass halos using the SZ effect will become more common as CMB telescopes become more sensitive, for now we depend on stacking, or averaging, multiple clusters that have been detected by other means. Stacking lets us use the SZ effect down to these lower masses, as it averages out contributions from the CMB and detector noise (Sehgal et al. 2013; Planck Collaboration et al. 2011; Hand et al. 2011).

At low redshift, optical surveys can identify clusters efficiently with multiband overdensity finders: e.g. MaxBCG (Koester et al. 2007), redMaPPer (Rykoff et al. 2014), and CAMIRA (Oguri 2014). At higher redshift, the infrared becomes an efficient avenue: e.g. MaDCoWS (Stanford et al. 2014), ISCS (Eisenhardt et al. 2008), IDCS (Stanford et al. 2012).

The SZ signal of low-richness, optically-selected clusters is less than expected from SZ mass–richness and weak lensing mass–richness relationships, which are usually calibrated with high-richness clusters. (Planck Collaboration et al. 2011; Draper et al. 2012; Sehgal et al. 2013; Saro et al. 2016). Several possible explanations for this discrepancy are radio or infrared point source contamination of the SZ signal, line-of-sight projections contaminating richness measurements, cluster miscentering, or a lower amplitude for the mass-richness relation. Solving this discrepancy is vital so that scaling relations for clusters, and therefore cluster physics, are understood over a wide mass range, allowing clusters to be used to their full cosmological potential.

In this work, we stack measurements of the SZ signal in data from the Atacama Cosmology Telescope (ACT) on cluster candidates selected from multifrequency imaging, including Spitzer data from the SHELA survey, by the redMaPPer algorithm. This sample is higher in redshift and lower in mass than many other samples. Using Herschel and Planck

data, we correct the stacked SZ decrement for contamination from dusty sources, and fit for a halo mass based on the cleaned SZ signal. We also compare the sample's average stellar mass and mass-richness relationship. We adopt the flat ΛCDM cosmology from the Planck 2013 data release (Planck Collaboration et al. 2014) with $H_0 = 67.9$ km s^{-1} Mpc^{-1}, $\Omega_m = 0.307$, $\Omega_\Lambda = 0.693$. The SZ signal and mass M_{500} is measured out to R_{500}, which is the radius enclosing 500 times the critical density at a given redshift.

This paper is organized as follows: In Section 2 we introduce the cluster sample, the ACT and ACTPol data, and the Herschel data used in this analysis. In Section 3 we describe the methods we used to analyze the data. These include the filtering and stacking procedures, calculation of the covariance matrices, and a discussion of the noise and signals that contribute to the stacked profiles. We describe our resulting multifrequency stacked profiles and discuss our methods for removing dust contamination. We describe our fitting procedure, including the SZ and pressure profile we use to translate our SZ signal into a cluster mass. In section 4, we present the results of our analysis and discuss how our SZ mass scales with stellar mass and richness. Section 5 concludes with a summary of the analysis and results.

2 DATA

2.1 Cluster Sample

The sample contains IR and optically selected redMaPPer cluster candidates from the Spitzer-HETDEX Exploratory Large Area survey (Papovich et al. 2016). SHELA is a 24 deg^2 IRAC survey in a low IR background region of Stripe 82, centered at a right ascension of $1^h22^m00^s$ on the celestial equator, and extending $\pm 6.5°$ in right ascension and $\pm 1.25°$ in declination. The SHELA survey region also includes DES *ugriz* imaging. Multiwavelength coverage in the same field includes SDSS, HETDEX, and DECam in the optical, NEW-FIRM in K-band, Herschel in the sub-mm, and ACT in the microwave.

The IR and optical imaging are passed through the redMaPPer algorithm (Rykoff et al. 2014), resulting in a catalog of 1082 groups and clusters with a richness $\lambda \geq 10$. Richness is a measure of how many galaxies belong to a cluster. In redMaPPer, it is defined as the sum of the membership probabilities for the galaxies within a cluster. We use clusters with richnesses $\lambda \geq 10$, and break these into three richness bins: $10 \leq \lambda < 20$, $20 \leq \lambda < 30$, and $\lambda \geq 30$. There are two are rich clusters already detected in the ACT SZ cluster sample (Hasselfield et al. 2013). We discard any SHELA clusters within 3 arcminutes of the ACT detected clusters before conducting a stacking analysis, leaving 840, 172, and 68 clusters in the lowest to highest richness bins, respectively. None of the remaining objects are detected individually in SZ by ACT, so their individual masses must be roughly $\leq 10^{14}$ $M_\odot$, ACT's approximate mass limit.

2.2 ACT Microwave Data

We use ACT data to measure the SZ decrement and null signals. ACT is a six-meter millimeter wave telescope that resides at an altitude of 5200 meters on Cerro Toco in the

Atacama Desert of Chile. It surveys the CMB with high resolution and sensitivity. The first generation of ACT observed during 2007-2010, and had three detector arrays at frequencies of 148, 220, and 277 GHz. These bands were chosen to study the SZ and capture the SZ decrement, null, and increment. ACT surveyed two regions on the sky, the "southern" and "equatorial" surveys. The southern survey covered 455 deg^2 and is centered on declination -53.5° (Marriage et al. 2011). The equatorial region overlaps with 270 deg^2 of Stripe 82 and the entire SHELA survey, covering 504 deg^2 and spanning from 20^{h}16^{m}00^s to 3^{h}52^{m}24^s in right ascension and -2°07′ to 2°18′ in declination (Hasselfield et al. 2013). The second generation of the experiment, ACTPol, was deployed in 2013 and has receivers at 90 and 148 GHz, with triple the sensitivity of ACT and is polarization sensitive. ACTPol has made observations in four deep field patches and one wider field and continues to take data (Naess et al. 2014). The wider "Deep 5/6" region overlaps with SHELA, covering 548 deg^2 and is centered on the celestial equator, expanding the area covered by ACT. In this work, we measure the SZ decrement using coadded, source subtracted, ACT temperature maps at 148 GHz from all observing seasons which overlap with the SHELA survey region: seasons 3–4 (2009 and 2010) of ACT and season 2 (2014) of ACTPol. The ACT maps have 0.495 arcmin pixels, while the ACTPol maps have 0.5 arcmin pixels. We use ACT maps that have been repixelized into the ACTPol pixelization to make coadded maps of all available data. We use 220 GHz data from seasons 3–4 of ACT, which is approximately the SZ null, to constrain contamination from thermal dust emission. These maps are also repixelized into the ACTPol pixelization. The beam sizes are 1.4 arcmin at 148 GHz, and 1.0 arcmin at 220 GHz.

2.3 Herschel Submillimeter Data

To measure dust emission from cluster member galaxies, we use far-IR data from the Herschel Stripe 82 (HerS) survey, which consists of maps at 250, 350, and 500 μm (or 1200, 857, 600 GHz) observed with *Herschel*/SPIRE (Viero et al. 2014). The survey covers 79 deg^2, spanning 13° to 37° in right ascension and -2° to +2° in declination. The SPIRE beams are 18.2, 25.2, and 36.3 arcsec at 1200, 857, 600 GHz, respectively. In addition to the maps, in this work we use the band-merged source catalog from the HerS team, which contains compact source flux densities and uncertainties in each band. The HerS team assumed sources are point-like and they identified them using the IDL software package STARFINDER (Diolaiti et al. 2000). They produced the band-merged catalog using the De-blended SPIRE Photometry (DESPHOT) algorithm, which uses sources from the 1200 GHz band as a prior for the other frequencies (Roseboom et al. 2010).

3 METHODS

3.1 SZ Profiles

The SZ signal can be expressed as a change in CMB temperature by:

$$\frac{\Delta T}{T_{CMB}} = y(\theta) f(x) \tag{1}$$

where $x = \frac{h\nu}{kT}$ and $f(x) = x(e^x + 1)/(e^x - 1) - 4$ contains the frequency dependence of the SZ effect. The Compton parameter y is proportional to pressure integrated along the line of sight (Sunyaev & Zeldovich 1972, 1970):

$$y = \frac{\sigma_T}{m_e c^2} \int dl\ P(\theta, l) \tag{2}$$

To translate our stacked temperature profile into a mass measurement, we use a universal pressure profile (UPP) of Arnaud et al. (2010) [A10], which is calibrated using low-redshift X-ray clusters from REXCESS (Böhringer et al. 2007). Arnaud et al. fit a generalized Navarro-Frenk-White profile which allows for a normalization that varies with mass and redshift and a mass-dependent deviation from self-similarity in the shape of the profile. In this model, the pressure at any radius r (or $x' \equiv r/R_{500}$) is:

$$P(r) = P_{500} \left[\frac{M_{SZ,500}}{3 \times 10^{14} h_{70}^{-1} M_\odot} \right]^{\alpha_P + \alpha'_p(x')} \mathbf{p}(x')\ h_{70}^2\ keV\ cm^{-3} \tag{3}$$

where P_{500} is the normalization of the pressure profile at a radius of 500 times the critical density at a given redshift:

$$P_{500} = 1.65 \times 10^{-3} E(z)^{8/3} \left[\frac{M_{500}}{3 \times 10^{14} h_{70}^{-1} M_\odot} \right]^{2/3} h_{70}^2 keV cm^{-3} \tag{4}$$

$\mathbf{p}(x')$ is the dimensionless universal pressure profile:

$$\mathbf{p}(x') = \frac{P_0}{(c_{500}x')^\gamma [1 + (c_{500}x')^\alpha]^{(\beta-\gamma)/\alpha}} \tag{5}$$

and $\alpha'_p(x')$ describes the deviation from self-similarity:

$$\alpha'_p(x') = 0.10 - (\alpha_P + 0.10) \frac{(x'/0.5)^3}{1. + (x'/0.5)^3} \tag{6}$$

with $\alpha_P = 0.12$. Using local clusters with XMM-Newton data, Planck Collaboration et al. (2013) update the best-fit parameters for the UPP to $[P_0, c_{500}, \gamma, \alpha, \beta] = [6.51, 1.81, 0.31, 1.33, 4.13]$, which we adopt in this paper.

3.2 Map Filtering and Stacking

Before stacking, we filter the maps using a conservative high-pass filter designed to remove large scale CMB fluctuations without altering the small scale cluster signal. To avoid bias, we design a filter independent of any assumed cluster shape. Our filter is a Fourier-space high-pass filter that we define in terms of its low-pass complement. The low-pass complement in real space is an apodized top-hat: unity inside 3′ radius and tapering to zero outside of 5′ with a cosine transition. Thus our high-pass filter removes the large scale features in the map, and barely touches small harmonic scales. Our filter is not matched to any specific cluster profile, and preserves the small-scale detector white noise. When compared, all maps, simulations, and model cluster profiles are subjected

to this same filter. We tested that our results are robust when introducing beam smoothing into our filter. The filter is the same high-pass filter used for the analysis, but convolved with the beam at 148 GHz to reduce pixel-scale white noise. This resulted in smoother, shallower profiles and mass measurements similar to those reported in this analysis, but with higher uncertainty as there was more bin to bin covariance.

The cluster candidates were not individually detected in SZ by ACT. To increase the signal-to-noise we stack, or average, observations of the clusters together into 30 annular bins, centered on the reported cluster positions, out to a radial separation of nine arcminutes. CMB and white noise fluctuations have zero mean, therefore stacking observations partially averages out these noise fluctuations. The center of each pixel determines where the measurement is binned.

We can write our stacked profiles as a sum of the beam-convolved signals $(b * P)(\theta)$ and noise (n):

$$P^{148} = b^{148} * (P^{SZ} + \alpha_{true} P^{dust,220} + n^{CMB}) + n^{det,148} \quad (7)$$
$$P^{220} = b^{220} * (P^{dust,220} + n^{CMB}) + n^{det,220} \quad (8)$$

The dust SED provides α_{true}, the amount of the 220 GHz dust signal that is present in the 148 GHz data. There is little SZ signal at 220 GHz, so we can use this profile to clean the 148 GHz stack by extrapolating the dust emission shape between bands by estimating α, which we measure by fitting a dust SED to the total flux density from sources in the HerS survey catalog. When we subtract the 220 GHz channel we deconvolve the beam at 220 GHz and reconvolve with the beam at 148 GHz.

3.3 Covariance Matrices

In the ACT frequencies, 148 and 220 GHz, the error in each annular bin of the stacked profile reflects the covariance introduced by CMB fluctuations, detector noise, and atmosphere. The covariance matrix is calculated by carrying out the same filtering and stacking procedure on 1600 simulations that model coadded ACT and ACTPol maps. To do this, we repixelize the ACT maps into the new ACTPol pixelization, and make coadded maps of all of the different seasons and arrays. We use the power spectra of the coadded maps to generate simulations which are then filtered. The covariance is largest in the small angle bins where there are few measurements to average down the noise. The correlation matrix for each richness bin at 148 GHz is shown in Figure 1.

Errors on the dust SED also figure into our final uncertainties. The HerS catalog includes 1σ uncertainties for the flux density of each source, which we use by averaging in quadrature for the SED fitting process.

3.4 Multifrequency Profiles

The stacked profiles for the two richness bins are shown in Figure 2. The profiles from ACT at 148 and 220 GHz are shown as well as the profiles from stacking on the HerS maps. The profiles at 148 GHz exhibit the decrement associated with the SZ effect at frequencies below 218 GHz. Around 218 GHz is the SZ null, and the stacks at 220 GHz contain little SZ signal. They do contain cluster-centered emission,

a fraction α_{true} of which will also be present at 148 GHZ, as well as CMB and noise. We will use this 220 GHz emission profile as a template to clean the 148 profile and estimate the true SZ signal. Also shown are profiles from stacking on the HerS maps at 500, 350, and 250 μm. The HerS stacks are shown for reference; we did not use them when fitting for a dust spectrum. Instead, we used the band-merged source catalog (Viero et al. 2014) to estimate α_{true}. The error bars on the stacked profiles result from stacking on the noise maps provided with the HerS data. The 220 GHz and Herschel stacks demonstrate that there is a signal from thermal dust emission within a few arcminute radius of the cluster centers. To test that our signal is not only a feature caused by the stacking procedure we stack on random positions in the ACT map, finding no signal on average. Figure 3 shows the results from stacking on random positions in the 148 GHz map, with each null stack accounting for the number of clusters in the different richness bins. The probability for χ^2 to exceed the null hypothesis is 0.02, 0.21, 0.92 respectively for the lowest to highest richness bin random null stacks.

3.5 Dusty Source Contamination

Emission from dusty sources and radio sources is a contaminant of the SZ signal (Aghanim et al. 2005). As seen in Figure 2, when stacking at 220 GHz (the SZ null) there is an excess signal, which we attribute to dust emission from cluster member galaxies. This positive emission will also be present at 148 GHz, where it fills in the SZ decrement, causing the sample to appear less massive. To correct for this, we use our 220 GHz stack as a template shape for dust contamination in the 148 GHz SZ signal, accounting for the different beam sizes. We extrapolate the amount of emission in the 220 stack to 148 GHz by determining the dust SED of sources near the clusters and calculating the ratio of the flux density at 148 relative to 220, which we denote as α. To determine α, we fit a graybody SED to sources from the HerS survey that are near to the clusters. We also look at the correlation in the CIB power spectra at 143 and 217 GHz from Planck, which gives us a similar result. After applying the correction for dust, the profile at 148 GHz becomes:

$$P^{corr,148} = b^{148} * \{P^{SZ} + (1-\alpha)n^{CMB} + (\alpha_{true} - \alpha)P^{dust}\}$$
$$+ n^{det,148} - b^{148}(b^{220})^{-1} * \alpha n^{det,220} \quad (9)$$

First, using the source catalog from the HerS survey (Viero et al. 2014), we fit a graybody SED

$$S(\nu) = A_{dust} \left(\frac{\nu(1+z)}{\nu_0}\right)^\beta \frac{(\nu(1+z))^3}{\exp(h\nu(1+z)/kT_{dust}) - 1} \quad (10)$$

for an overall amplitude, A_{dust}, and dust temperature, T_{dust}, using the total contribution of all the sources within a fixed angular distance from the clusters. We fix the emissivity spectral index β to 1.5, ν_0 to 100 GHz, and the redshift to the average redshift for each of the richness bins. Magnelli et al. (2014) find that setting β to 1.5 is a good estimate when fitting spectra without enough information to constrain it, and note that it may cause T_{dust} to be slightly overestimated. Furthermore, when fitting for a stacked SZ plus greybody spectrum, Erler et al. (2017) found that the choice of β had little influence on the measured SZ signal, and use $\beta = 1.5$ to obtain their main results. We ran our pipeline using β
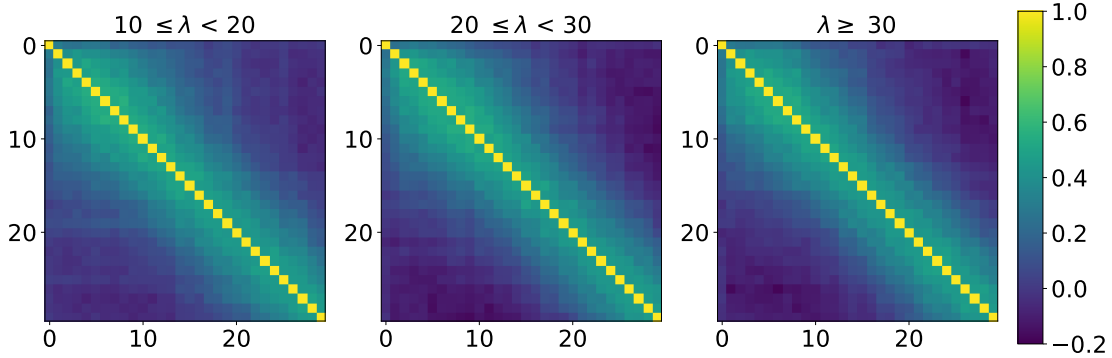
Figure 1. Correlation matrices for the stacked pressure profiles at 148 GHz for the three richness bins, $10 \geq \lambda < 20$ (left), $20 \leq \lambda < 30$, and $\lambda \geq 30$ (right). They are obtained by stacking on 1600 ACT simulations which contain correlations introduced by CMB fluctuations, detector and atmospheric noise for the different observing seasons of ACT used in this analysis.

= 1.4 and 1.6 to see how β affects our results. We found that varying β did not significantly affect the mass measurements, the differences were much less than 1σ. To test whether the angular aperture within we include sources affects our SED measurement, we fit the spectrum to sources within a range of apertures. We also tested whether fixing a reasonable value for T_{dust} and fitting for an amplitude and redshift affects the results. Including sources out to varying radii, between 1 and 11 arcminutes from the cluster center, we see similar 220 to 148 GHz extrapolation parameter α. Fixing T_{dust} and allowing the redshift to vary also gives a similar extrapolation, both fitting methods result in realistic values for T_{dust} or z. The only information we need is the SED between 220 and 148 GHz, which is used to calculate α. This is given by the shape of the dust SED, meaning the exact fitted values for the amplitude, T_{dust}, or z are not as important to the analysis as long as they are realistic. We report results fitting sources with an 11' aperture in Table 1. We find a value of 0.28 for α, meaning that 28% of the emission present in the stacked profile at 220 GHz is carried over to 148 GHz.

$$\mathcal{D}_\ell^{\text{CIB}_{143\times143}} = A_{143}^{\text{CIB}} \left(\frac{\ell}{3000}\right)^{\gamma^{\text{CIB}}}, \quad \mathcal{D}_\ell^{\text{CIB}_{217\times217}} = A_{217}^{\text{CIB}} \left(\frac{\ell}{3000}\right)^{\gamma^{\text{CIB}}}, \tag{11}$$

which are translated to ACT frequencies using:

$$\mathcal{D}_\ell^{\text{CIB}_{\nu_i\times\nu_j}} = \mathcal{D}_{3000}^{\text{CIB}_{\nu_{i0}\times\nu_{j0}}} \left(\frac{g(\nu_i)g(\nu_j)}{g(\nu_{i0})g(\nu_{j0})}\right)\left(\frac{\nu_i\nu_j}{\nu_{i0}\nu_{j0}}\right)^{\beta_d} \frac{B_{\nu_i}(T_d)}{B_{\nu_{i0}}(T_d)} \frac{B_{\nu_j}(T_d)}{B_{\nu_{j0}}(T_d)} \tag{12}$$

where $B_\nu(T_d)$ is the Planck function, $g(\nu) = [\partial B_\nu(T)/\partial T]^{-1}|_{T_{\text{CMB}}}$, and the parameters β_d and T_d are fixed at 2.20 and 9.7 K, respectively. We then use the ratio in the power spectra to convert our 220 signal into a correction for the 148 GHz stack. We find with this method that 28 ± 7% of the signal at 220 is carried over into the 148 stack, in agreement with the value of α we found from the Herschel fitting.

3.6 Radio Source Contamination

Radio sources have been found to preferentially reside in clusters of galaxies and are often associated with emission from the cluster member galaxies (Holder 2002; Lin & Mohr 2007; Coble et al. 2007; Lin et al. 2009). Similarly to the process of measuring dust emission, we look for radio sources within 11' and model their emission at 148 and 220 GHz. We use sources from the NVSS survey at 1.4 GHz (Condon et al. 1998). We find no bright sources within this sample after our initial pruning, and extrapolate the stacked synchrotron emission profile using spectral indices −0.5, −0.7, and −0.9. We find emission in the ACT bands that is much lower than the SZ signal, and therefore we make no further correction.

4 RESULTS

We use a Monte Carlo formalism to fit for M_{500} from our stacked profile at 148 GHz. We then use richness information available from the IR and optical data to compare to other works.

4.1 Mass Fitting

To take into account how the dust correction affects the mass fitting, we simultaneously fit for a dust SED and an SZ profile. We use a Gaussian likelihood and the affine-invariant Markov Chain Monte Carlo code *emcee* (Foreman-Mackey et al. 2013). The fit parameters are the average cluster mass M_{500}, an overall DC offset for the stacked profile p_0, an amplitude for the graybody SED A_{dust}, and a dust temperature T_{dust}. We fix the redshift dependence of the dust spectrum and SZ signal to the average redshift for each sample, z = 0.80, 0.73, and 0.70, for the lowest and highest richness bins. We apply a flat prior for values within the following ranges: $0M_\odot < M_{500} < 10^{15}M_\odot$, $-10\mu K < p_0 < +10\mu K$, 0 mJy/Hz^3 < A_{dust} < 0.1 mJy/Hz^3, 3K < T_{dust} < 500K. The HerS flux densities are used to sample the graybody SEDs. The ratio of the SED at 148 and 220 GHZ is used to calculate α, which gives our dust correction by allowing us to extrapolate the 220 GHz profile to 148 GHz, assuming that the profile at 220 GHz is dominated by dust emission. The extrapolated dust signal is subtracted from the raw stack at 148 GHz.
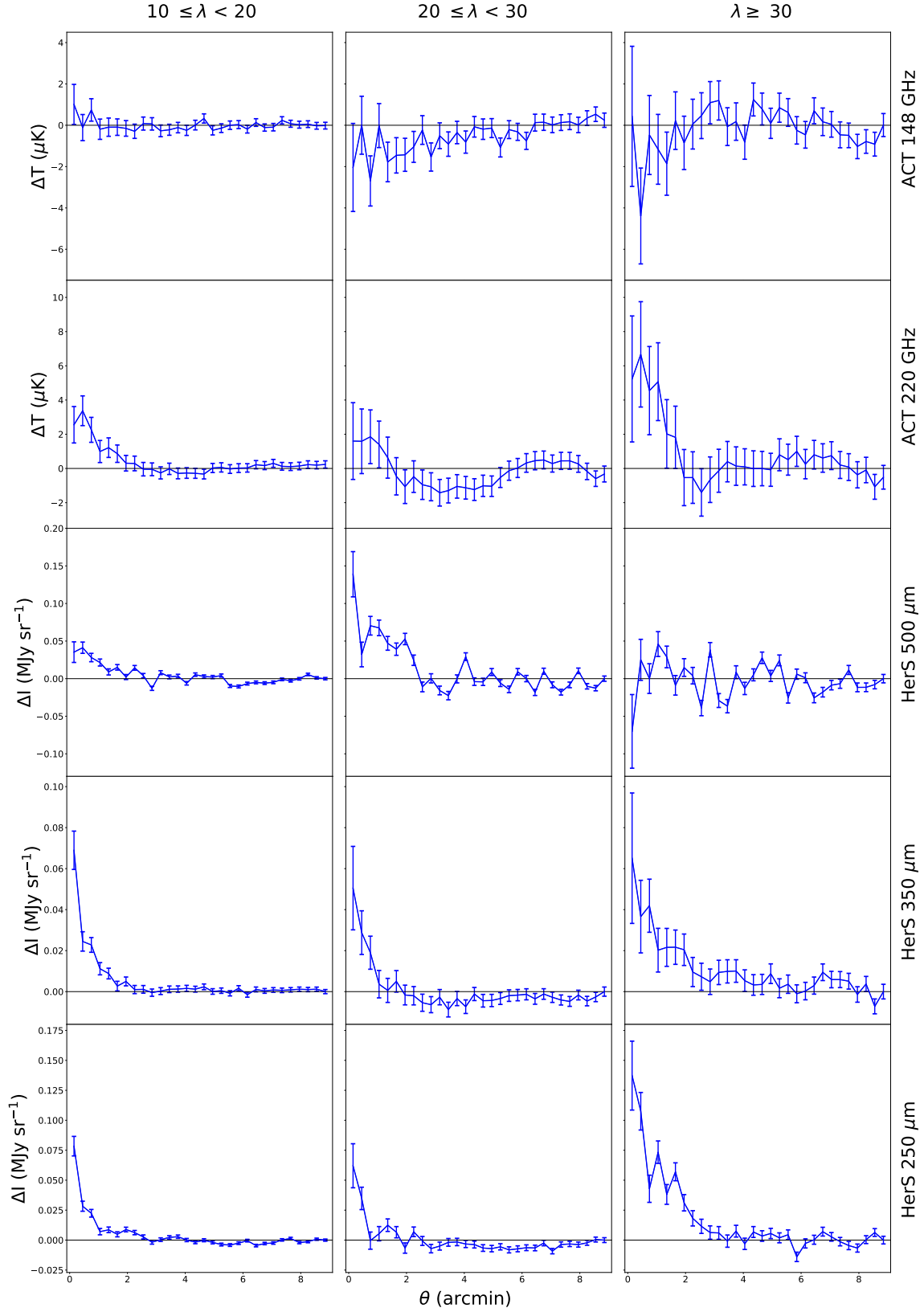
Figure 2. Stacked profiles for all 5 bands used in this analysis for the three richness bins: ACT 148, 220 GHz and HerS 500, 350, 250 μm. The main contributions to the profile at 148 GHz are the SZ signal, plus some signal from thermal dust emission. 220 GHz is near the SZ null, and contains emission which contaminates the signal at 148 GHz. The Herschel bands (500, 350, 250 μm) trace thermal dust emission in the clusters. There are 840, 172, and 68 clusters in each richness bin, from lowest to highest, respectively.

Table 1. Best-fit parameters for fitting an SZ profile in two ways: correcting for dust emission, and neglecting dust contamination.

	$10 \leq \lambda < 20$		$20 \leq \lambda < 30$		$\lambda \geq 30$	
	Dust corr.	No dust corr.	Dust corr.	No dust corr.	Dust corr.	No dust corr.
M_{500} (10^{13} M$_\odot$)	1.0 ± 0.6	0.9 ± 0.3	2.3 ± 1.2	1.7 ± 0.8	5.6 ± 1.6	3.7 ± 1.5
p_0 (μK)	-0.06 ± 0.10	-0.02 ± 0.09	0.07 ± 0.21	-0.01 ± 0.18	-0.17 ± 0.33	-0.23 ± 0.31
A_{dust} (10^{14}Jy/Hz^3)	3.66 ± 0.02	-	4.39 ± 0.06	-	5.10 ± 0.10	-
T_{dust} (K)	29.1 ± 0.1	-	28.0 ± 0.1	-	27.0 ± 0.2	-

Resulting fit parameters for the two richness bins. The first column for each richness bin shows results from fitting for a dust SED simultaneously with the SZ profile to remove dust emission, fixed at the average redshift for each sample (for $1 - b = 1$). The second column lists the results if we neglect the dust correction (for $1 - b = 1$) and fit an SZ profile directly to the original stacked profile.
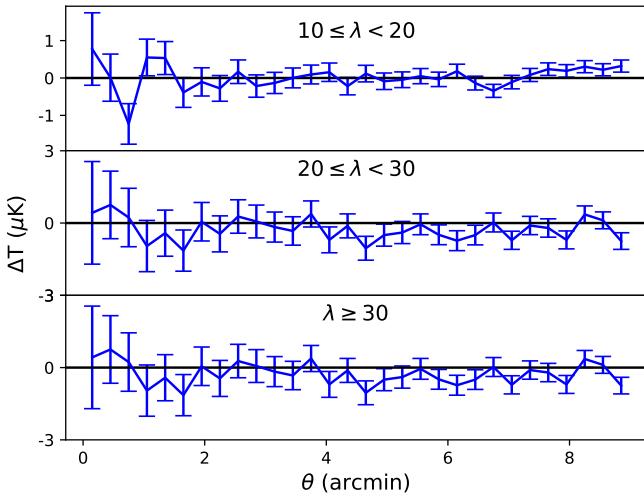
Figure 3. Stacking null test at 148 GHz. Random positions for the number of clusters in each richness bin are stacked on to test that there is no SZ signal in places unassociated with clusters.

The UPP with updated parameters is integrated to calculate the SZ signal $y(\theta)$, which is convolved with the ACT beam and translated into a temperature profile, $\Delta T(\theta)$, that is fit to our dust-subtracted stacked profile.

Figures 4 and 5 show the results from fitting the stacked profile and IR data to a dust SED and cleaned SZ profile. Figure 4 shows the cleaned SZ profiles along with the most likely profiles from the MCMC chains. The light green area encompasses 68% of the models from the MCMC chains in each bin. For both richness bins, Figure 5 shows the parameter contours for M_{500}, redshift, a DC offset in the 148 GHz stack, a dust spectrum amplitude, and a dust temperature from the MCMC chains. The lower tails of the distributions for M_{500} are pushing against the prior, which is zero. None of the parameters seem correlated except the dust amplitude and temperature, which are anti-correlated. The fit parameters are summarized in Table 1, which show results from simultaneously fitting a dust SED and SZ profile to the stacked 148 GHz data and fitting an SZ profile directly to the data while correcting and neglecting to correct for dust. Neglecting to correct for dust decreases the mass by 10% for $10 \leq \lambda < 20$, 26% for $20 \leq \lambda < 30$, and 34% for $\lambda \geq 30$. We
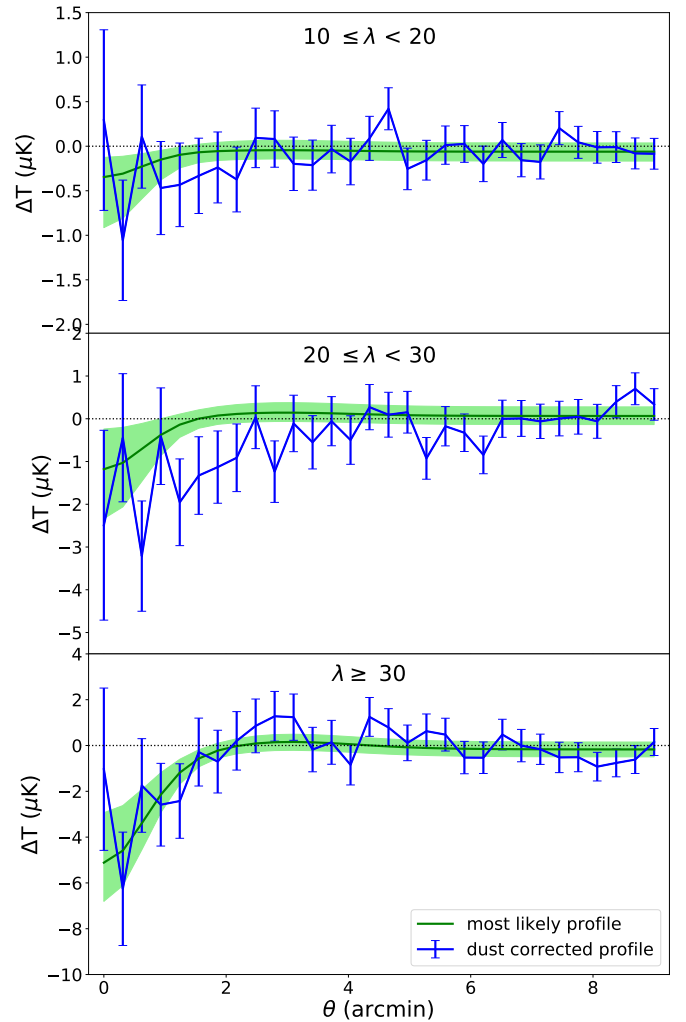
Figure 4. Results from fitting for a cleaned SZ profile for the three richness bins. The blue line is the stacked profile after taking into account the dust correction, given by α and the profile at 220 GHz. The green line is the result from the MCMC chains. The green contours bound the models in the chain between the 16th and 84th percentiles in each angular bin.
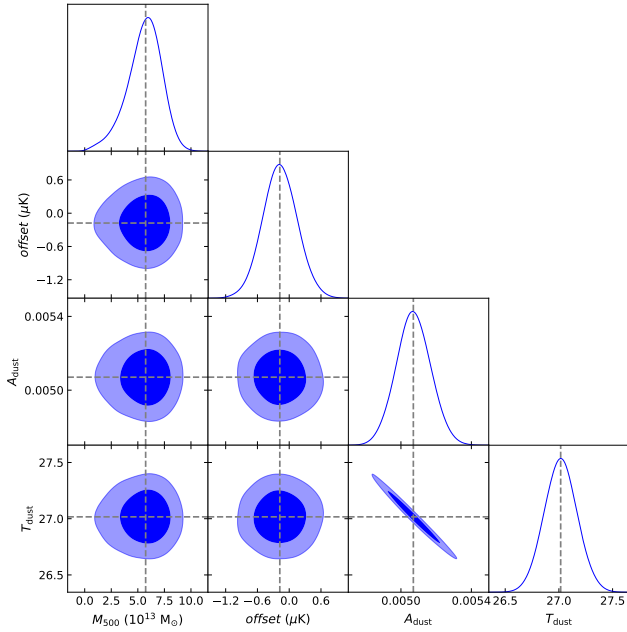
Figure 5. Parameter contours from MCMC chains for the highest richness bin, $\lambda \geq 30$. The grey dashed lines pass through the mean value from the probability distributions for each parameter. The dust amplitude and temperature are anti-correlated in both richness bins.

use the random stacks from Figure 3 to test what mass our pipeline measures when there is no signal. Fitting without a dust correction results in probabilities of measuring a mass that pushes up against the lower limit of the prior, zero. **At 95% confidence, the upper limit of the distributions are 2.0 $\times 10^{13} M_\odot$ and 3.1 $\times 10^{13} M_\odot$, for the lower and higher richness bins. These masses measured for the lower richness bin are close to the values measured in the main analysis, showing that there is only evidence of the SZ signal for these clusters.** When also measure the SZ mass of only the dust correction, using the data stack at 220 GHz as shown in Figure 2 (the case of zero SZ signal), and measure masses of $(1.7^{+0.9}_{-0.7}) \times 10^{13} M_\odot$, $(2.1^{+1.2}_{-2.0}) \times 10^{13} M_\odot$, and $(3.2^{+1.8}_{-1.9}) \times 10^{13} M_\odot$ for the lower and higher richness bins respectively. **In terms of Y_{500}, this means that 75% ± 84% of the SZ signal in the lowest richness bin, 60% ± 67% in the middle bin, and 52% ± 40% of the SZ signal in the highest richness bin is filled in by dust emission.** Figure 6 shows the probability distributions of measuring Y_{500} for these two cases, and is meant to demonstrate how the probabilities are distributed and show that the dust correction makes a large portion of the measured SZ signal.

4.2 Mass Bias

The relation between SZ signal and cluster mass, Y–M, is measured using x-ray derived cluster masses (Arnaud et al. 2010; Andersson et al. 2011), but there are several effects that cause these x-ray mass measurements to be biased low. Clusters are assumed to be in hydrostatic equilibrium (HE), but non-thermal pressure support from turbulence and ran-
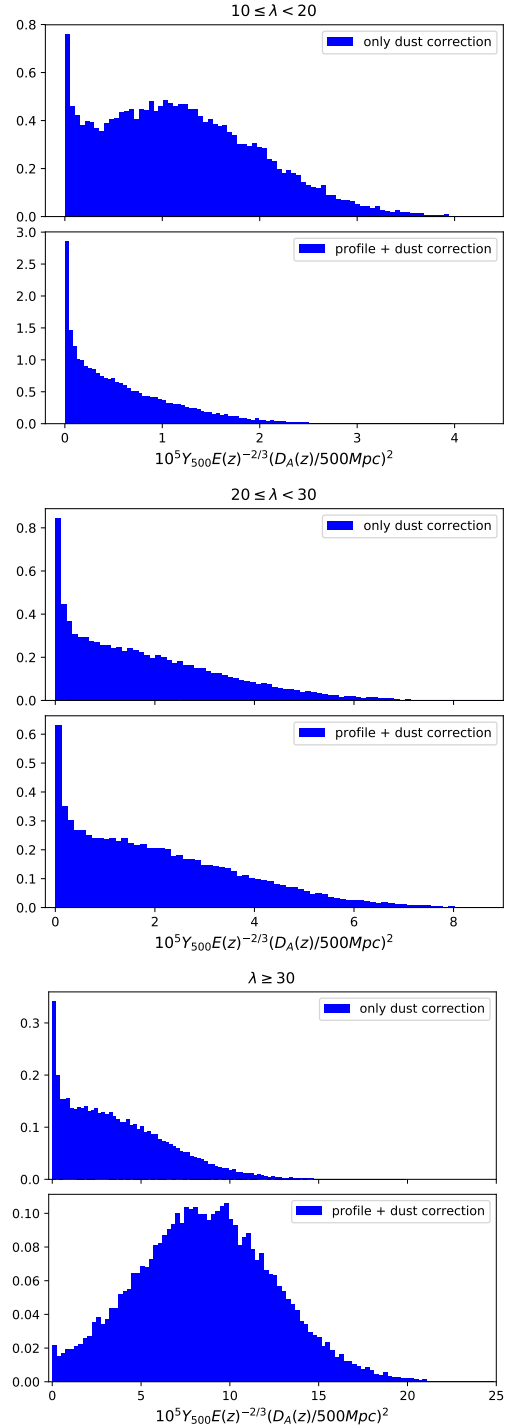
Figure 6. Probabilities of measuring Y_{500} for two different cases, for each richness bin. The upper plots for each richness bin are the distributions for Y_{500} of only the dust correction (the case of no SZ signal at 148 GHz). The lower plots for each richness bin are the distributions of Y_{500} for the dust corrected profiles. For each richness bin, it can be seen that the dust correction is a significant portion of the total mass measurement.
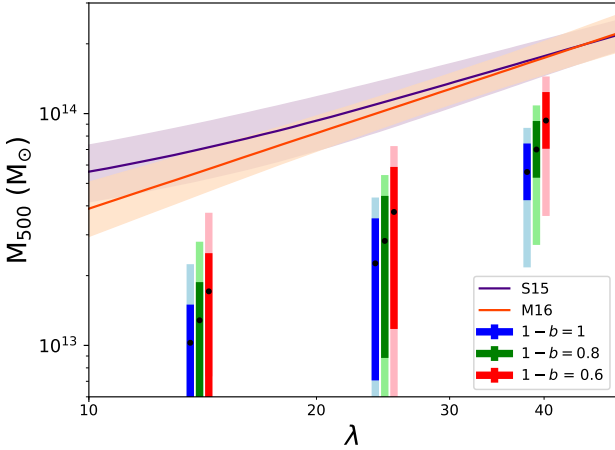
Figure 7. Comparison with redMaPPer mass-richness relations. The red line is the mass-richness relation of Melchior et al. (2016) which was calibrated using weak-lensing masses of redMaPPer clusters in DES data. The blue line is the mass-richness relation of Saro et al. (2015) which was calibrated using SZ masses of redMaPPer clusters in SPT. The data points for the results for the masses of the SHELA clusters in each richness bin with different values for the amount of hydrostatic mass bias, $1 - b$. The data point for the case of $1 - b = 0$ is plotted at the average richness in each bin. The other two points are slightly offset from the average richness for the sake of clarity. For the two models, the average redshift of all the clusters, $z = 0.78$, is used.

dom motions move the clusters away from perfect HE. Single temperatures are also fit to x-ray data, but subregions with higher temperatures can be present and get averaged down, resulting in a bias toward measuring a lower temperature and therefore mass. The bias between the true mass and the mass measured by the SZ effect is $1 - b = M/M_{\rm true}$. The precise value for $1 - b$ is not well understood and could have a large range of values(Planck Collaboration et al. 2014). In Planck Collaboration et al. (2014), $1 - b$ is fixed at 0.8 as an estimation of the possible value. Battaglia et al. (2016) measured the mass bias for high signal to noise clusters from the ACT equatorial survey, using weak-lensing data from the Canada-France-Hawaii telescope stripe 82 survey. They found that $1 - b$ is 0.98 ± 0.28 and 0.87 ± 0.27 when fitting the weak-lensing mass using models based on simulations and an NFW profile, respectively. There have been several other measurements of $1-b$, with values ranging from 0.58 to 0.95 (von der Linden et al. 2014; Hoekstra et al. 2015; Smith et al. 2016; Planck Collaboration et al. 2016). When comparing our measured M_{SZ} to cluster mass scaling relations, we use the values: $1-b = 1$, 0.8, and 0.6. We choose these values to sample the range of values that have been measured, so that we can demonstrate how much different amounts of hydrostatic mass bias could affect our mass measurements.

4.3 Richness to Mass Scaling

Accurately measuring the masses of cluster halos is necessary for clusters to be used for cosmology, making it is vital to map out the relation between mass and the cluster observables, such as the SZ signal and richness. It is important

to compare different observable to mass relations which have different biases and contaminating factors to test if predicted scaling relations hold. Multiple studies have seen that the SZ observable has some feature that causes a lower SZ signal than predicted when λ–M relations are extrapolated to lower mass objects (Planck Collaboration et al. 2011; Draper et al. 2012; Sehgal et al. 2013; Saro et al. 2016), and we explore that possibility here.

Saro et al. (2016) [S16] took a sample of DES redMaP-Per clusters with weak lensing masses and measured their SZ signal in SPT (South Pole Telescope) data in multiple richness bins. They used weak lensing masses and their own richness-mass model (Saro et al. 2015) [S15], which they inverted into a mass-richness model and extrapolated to measure Y_{500}. They ran two cases, using their own $M_{500} - Y_{500}$ model and using the model from A10. They compared the Y_{500} expected in each richness bin to what was measured from stacking on the SPT SZ map. They found that for clusters with $\lambda > 80$, Y_{500} is consistent with their model and smaller by 0.61±0.12 from A10. For $20 < \lambda < 80$, they found that the SZ signal was smaller by a factor of 0.2-0.8, with higher richness bins and the S15 $M_{500} - Y_{500}$ showing better agreement. They explained this with a richness dependent bias, caused by contamination of the SZ and richness observables or bias in estimated halo mass, e.g. contamination of richness from line of sight projections, contamination of the SZ observable, a larger offset in SZ-optical centering than accounted for, or a larger intrinsic scatter in richness-mass relation at lower richness. In Figure 7 we compare our results to the M_{500}-λ relation of S16. To make this comparison, we need to take into account that they have modeled $P(\lambda|M_{500})$ as opposed to $P(M_{500}|\lambda)$. Their model is a log-normal distribution with mean:

$$\langle \ln \lambda | M_{500}, z \rangle = \ln A_\lambda + B_\lambda \ln\left(\frac{M_{500}}{3 \times 10^{14} h^{-1} {\rm M}_\odot}\right) + C_\lambda \ln\left(\frac{E(z)}{E(z = 0.6)}\right) \tag{13}$$

To invert this relation, we perform the following operation:

$$P(M_{500}|\lambda^{\rm obs}) \propto P(M_{500}, z) \int P(\lambda^{\rm obs}|\lambda) \, P(\lambda|M_{500}, z) \, d\lambda \tag{14}$$

where $P(\lambda|M_{500}, z)$ is the SPT probability marginalized over the fit parameters A_λ, B_λ, and C_λ. $P(\lambda^{\rm obs}|\lambda)$ is the probability for observing a value for the richness given the true richness, and $P(M_{500}, z)$ is proportional to the halo mass function.

Melchior et al. (2016) [M16] measure the $P(M_{200}|\lambda)$ for redMaPPer clusters in DES. For comparison, we translate their model in terms of M_{200m} to M_{500c}, where m denotes the density contrast relative to the mean matter density and c is relative to the critical density at that redshift. Although we do not compare our data to other redMaPPer richness-mass models, we note that there is good agreement with relations from S16 and Simet et al. (2017) [S17], which calibrates the mass-richness relation for redMaPPer clusters in SDSS.

We compare the models from S16 as they used redMaP-Per clusters with masses derived using the SZ effect, as are ours, and M16 as their redMaPPer richnesses are from data observed by DECam, similarly to the SHELA data. Our data are plotted against these models in Figure 7. For the SHELA sample, M_{500} from SZ profile fitting and the average richness per bin are used. We tested different ways to represent our richness bins, such as using mass-weighted and SZ-weighted

average richnesses, but find that they are similar to the mean richness per bin, so we simply use the mean value. The average richnesses for the lower and higher richness bins are approximately 14, 24, and 38. Similarly to the results of S16, we find that our clusters are less massive than predicted. Relative to the model of S16: Our masses are 3.8 times smaller for the lower richness bin, and 2.5 times smaller for the higher richness bin, without accounting for hydrostatic mass bias. Relative to M16: Our masses are 2.9 times smaller for the lower richness bin, and 2.2 times smaller for the higher richness bin. If accounting for a hydrostatic mass bias of 0.8, our masses are 3.0 and 2.0 times smaller than S16 and 2.3 and 1.8 times smaller than M16, respectively for the lower and richness bin. As is shown in Figure 7, a large value for hydrostatic mass bias is necessary to reconcile our data with the richness-based mass models. It would not be possible for an error in the richness to cause this large of a discrepancy, therefore there must be other factors in play. Several reasons are more contamination in the SZ signal than we have accounted for, mass-richness relations being incorrect at low richness, and differences in the meaning of the richnesses themselves because the objects are higher redshift and include IR data in the cluster finding algorithm.

5 DISCUSSION

We have presented the analysis of stacked SZ profiles for a sample of IR and optically-selected clusters from the Spitzer-HETDEX Exploratory Large Area survey. We binned this sample into three richness bins: $10 \leq \lambda < 20$, $20 \leq \lambda < 30$ and $\lambda \geq 30$. There are 840, 172, and 68 clusters in the richness bins, from lowest to highest. At the SZ null (220 GHz), the stacked profiles both exhibited an excess signal, which we attributed to thermal dust emission from cluster member galaxies. We tested for radio emission as well, but found no significant contribution. For each bin, we fit for a dust SED using sources from the Herschel Stripe 82 survey catalog to extrapolate the dust SED from 220 GHz to 148 GHz, so that we could use the 220 GHz stacked profile as a template to clean the 148 GHz stack. As a check, we compared the ratio of dust emission at 148 and 220 GHz from the dust SED to the extrapolation from the Planck CIB power spectrum. We found a similar result for both methods, which is that $\sim 28\%$ of thermal dust emission at 220 GHz is also present at 148 GHz. After removing dust emission, we fit the cleaned stack at 148 GHz to an SZ profile using a universal galaxy cluster pressure profile to translate our temperature decrement to a halo mass. For each richness bin, we used an MCMC procedure that simultaneously fit for the SZ profile and dust SED while fixing redshift to the average of the cluster sample. We compared the chains with and without the dust correction, and found for the lower richness bin, $10 \leq \lambda < 20$, that correcting for dust emission increases the M_{500} measurement by a factor of 1.9. For the higher richness bin, $\lambda \geq 20$, M_{500} increases by a factor of 2.2. This translates to $80\% \pm 65\%$ of the SZ signal in the lower richness bin and $65\% \pm 40\%$ of the SZ signal in the higher richness bin being filled in by dust emission.

The SHELA cluster catalog obtains richnesses from the redMaPPer algorithm. We used this information, along with our SZ masses, to compare the SHELA clusters to other works in the literature. We compared our mass and richness data to two models which have mapped out the richness-mass relation for redMaPPer clusters. SZ measurements of optically-selected clusters are generally smaller than expected when comparing to mass-richness models, and the SHELA clusters follow this trend. We found that our data are 3.8 and 2.5 times smaller than predicted, respectively for the lower and higher richness bins relative to the model of S15. In comparison to the model of M16, our masses are 2.9 and 2.2 times smaller for the lower and higher richness bins, respectively.

This is a step toward studying characteristics of galaxy clusters over a range of redshifts and masses. In the future, wider and deeper coverage by Advanced ACT and the Simons Observatory will allow this study by observing a large number of clusters in five frequency bands, and by increasing overlap with optical surveys such as BOSS, HSC, DES, DESI, and LSST (De Bernardis et al. 2016). In the future it may be fruitful to repeat this type of analysis for more infrared-selected objects, using the Spitzer IRAC Equatorial Survey (SpIES, Timlin et al. 2016). SpIES is shallower than SHELA, but larger, covering an adjacent ~115 square degrees of Stripe 82.

REFERENCES

Aghanim N., Hansen S. H., Lagache G., 2005, A&A, 439, 901
Andersson K., et al., 2011, ApJ, 738, 48
Arnaud M., Pratt G. W., Piffaretti R., Böhringer H., Croston J. H., Pointecouteau E., 2010, A&A, 517, A92
Battaglia N., et al., 2016, J. Cosmology Astropart. Phys., 8, 013
Birkinshaw M., 1999, Phys. Rep., 310, 97
Böhringer H., et al., 2007, A&A, 469, 363

Carlstrom J. E., Holder G. P., Reese E. D., 2002, ARA&A, 40, 643

Coble K., et al., 2007, AJ, 134, 897

Condon J. J., Cotton W. D., Greisen E. W., Yin Q. F., Perley R. A., Taylor G. B., Broderick J. J., 1998, AJ, 115, 1693

De Bernardis F., et al., 2016, in Observatory Operations: Strategies, Processes, and Systems VI. p. 991014 (arXiv:1607.02120), doi:10.1117/12.2232824

Diolaiti E., Bendinelli O., Bonaccini D., Close L., Currie D., Parmeggiani G., 2000, A&AS, 147, 335

Draper P., Dodelson S., Hao J., Rozo E., 2012, Phys. Rev. D, 85, 023005

Eisenhardt P. R. M., et al., 2008, ApJ, 684, 905

Erler J., Basu K., Chluba J., Bertoldi F., 2017, preprint, (arXiv:1709.01187)

Foreman-Mackey D., Hogg D. W., Lang D., Goodman J., 2013, PASP, 125, 306

Giodini S., Lovisari L., Pointecouteau E., Ettori S., Reiprich T. H., Hoekstra H., 2013, Space Sci. Rev., 177, 247

Hand N., et al., 2011, ApJ, 736, 39

Hasselfield M., et al., 2013, J. Cosmology Astropart. Phys., 7, 008

Hoekstra H., Herbonnet R., Muzzin A., Babul A., Mahdavi A., Viola M., Cacciato M., 2015, MNRAS, 449, 685

Holder G. P., 2002, ApJ, 580, 36

Koester B. P., et al., 2007, ApJ, 660, 221

Laganá T. F., Martinet N., Durret F., Lima Neto G. B., Maughan B., Zhang Y.-Y., 2013, A&A, 555, A66

Lin Y.-T., Mohr J. J., 2007, ApJS, 170, 71

Lin Y.-T., Partridge B., Pober J. C., Bouchefry K. E., Burke S., Klein J. N., Coish J. W., Huffenberger K. M., 2009, ApJ, 694, 992

Liu J., et al., 2015, MNRAS, 448, 2085

Magnelli B., et al., 2014, A&A, 561, A86

Marriage T. A., et al., 2011, ApJ, 731, 100

Melchior P., et al., 2016, preprint, (arXiv:1610.06890)

Naess S., et al., 2014, J. Cosmology Astropart. Phys., 10, 007

Oguri M., 2014, MNRAS, 444, 147

Papovich C., et al., 2016, ApJS, 224, 28

Planck Collaboration et al., 2011, A&A, 536, A12

Planck Collaboration et al., 2013, A&A, 550, A131

Planck Collaboration et al., 2014, A&A, 571, A16

Planck Collaboration et al., 2016, A&A, 594, A24

Roseboom I. G., et al., 2010, MNRAS, 409, 48

Rykoff E. S., et al., 2014, ApJ, 785, 104

Saro A., et al., 2015, MNRAS, 454, 2305

Saro A., et al., 2016, preprint, (arXiv:1605.08770)

Sehgal N., et al., 2013, ApJ, 767, 38

Simet M., McClintock T., Mandelbaum R., Rozo E., Rykoff E., Sheldon E., Wechsler R. H., 2017, MNRAS, 466, 3103

Smith G. P., et al., 2016, MNRAS, 456, L74

Stanford S. A., et al., 2012, ApJ, 753, 164

Stanford S. A., Gonzalez A. H., Brodwin M., Gettings D. P., Eisenhardt P. R. M., Stern D., Wylezalek D., 2014, ApJS, 213, 25

Sunyaev R. A., Zeldovich Y. B., 1970, Comments on Astrophysics and Space Physics, 2, 66

Sunyaev R. A., Zeldovich Y. B., 1972, Comments on Astrophysics and Space Physics, 4, 173

Timlin J. D., et al., 2016, ApJS, 225, 1

Viero M. P., et al., 2014, ApJS, 210, 22

Voit G. M., 2005, Reviews of Modern Physics, 77, 207

von der Linden A., et al., 2014, MNRAS, 443, 1973

This paper has been typeset from a TEX/LATEX file prepared by the author.